Nanograin-Twin-Nanograin Alternating Composite Structure Enable Improved Cross-Interface Cu—Cu Bonding at Low Thermal Budgets

Cong Chen, Helios Y. Li, Gangqiang Peng, Zeyang Zheng, Erqian Dong, Jianwen Zhong, Chuan He, Yi Wang, Jia-Syuan Chang, Zhuofei Gan, Jinwei Gao,* Yu-Ting Huang,* Chih-Ming Chen,* and Shien-Ping Feng*

Chip stacking using through-silicon via (TSV) and direct copper-to-copper (Cu—Cu) bonding technology has emerged as a superior solution to overcome the limitations of Moore's law. However, conventional approaches face a fundamental trade-off: coarse-grained Cu requires high bonding temperatures (>300 °C), while nanograined Cu is unstable and tends to coarsen even at room temperature after electroplating. Here, this paradigm is broken through a unique composite copper (comp-Cu) architecture featuring alternating nanograin (ng—Cu) and (111)-oriented nanotwin (nt—Cu) domains. The nt—Cu domains, stabilized by coherent twin boundaries (CTBs), suppress room-temperature grain growth (2% resistance drifts over 15 days), while ng—Cu regions enable rapidly grain growth at 170 °C. This dual functionality facilitates atomic bridging across interfaces via two synergistic pathways: 1) grain-boundary-diffusion-dominated ng—Cu recrystallization and 2) low-activation-energy surface migration along nt—Cu (111) planes. The resulting bonded joints achieve enhanced mechanical and electrical performance: 56.4±3.6 MPa shear strength (52% > coarse Cu), 258 h electromigration lifetime (6.45× > conventional), and 3.1% resistance drift after 1,000 thermal cycles (−16–160 °C). The work not only provides a practical solution for low-thermal-budget 3D packaging but also establishes a paradigm for designing metastable composites that reconcile traditionally incompatible properties.

1. Introduction

Recently, chip stacking has emerged as a promising technology in advanced microelectronic packaging to overcome the physical limits of Moore's law.[1,2] Through-silicon via (TSV) and micro-bump are employed to shorten the wiring between chips, offering high interconnect density, small form factor, low power consumption, and high performance.[3] In industrial applications, micro solder bumps are widely used for chip-level bonding; however, their pitch is constrained to ≈20 µm because the adjacent micropumps may touch each other if the pitch is too small during thermal compression bonding or reflow.[4,5] To overcome these challenges, direct Cu—Cu bonding has been proposed as an alternative, enabling further pitch reduction.[6,7]

Conventional coarse-grained Cu direct bonding typically requires high temperatures (>300 °C) to overcome surface oxide barriers and activate bulk

C. Chen, G. Peng, C. He, Y.-T. Huang, S.-P. Feng
Department of Systems Engineering
City University of Hong Kong
Tat Chee Avenue, Hong Kong, Hong Kong SAR 999077, P. R. China
E-mail: vivian.huang@doctech-group.com; tony.feng@cityu.edu.hk
C. Chen, H. Y. Li, Z. Zheng, E. Dong, J. Zhong, Y. Wang, Z. Gan
Department of Mechanical Engineering
The University of Hong Kong
Pokfulam Rd, Hong Kong, Hong Kong SAR 999077, P. R. China
J. Gao
Centre for Advanced Optoelectronics
School of Intelligent Manufacturing and Future Energy
Gannan Normal University
No. 1 Shida South Road, Ganzhou, Jiangxi 341000, P. R. China
E-mail: gaojinwei@gnnu.edu.cn

Y.-T. Huang
Doctech HK Limited
Hong Kong Science and Technology Parks
Hong Kong, Hong Kong SAR 999077, P. R. China
J.-S. Chang, C.-M. Chen
Department of Chemical Engineering
National Chung Hsing University
No. 145, Xingda Road, Taichung 402202, Taiwan
E-mail: chencm@nchu.edu.tw
C.-M. Chen
Innovation and Development Center of Sustainable Agriculture (IDCSA)
National Chung Hsing University
No. 145, Xingda Road, Taichung 402202, Taiwan

**ADVANCED
SCIENCE NEWS**

www.advancedsciencenews.com

**small
methods**

www.small-methods.com

diffusion,[6,8–10] but such thermal aggression fundamentally conflicts with the integration of temperature-sensitive components (e.g., advanced Dynamic Random-Access Memory(DRAM), organic substrates) and introduces reliability concerns such as misalignment, residual thermal stress, and compromised reliability.[11] Recent efforts have focused on reducing the thermal budget for Cu—Cu bonding. For instance, surface-activated bonding techniques utilize Ar ion beams under ultra-high vacuum (UHV) to clean Cu surfaces and remove oxides, enabling bonding at lower temperatures.[12,13] However, such UHV-dependent methods face scalability challenges in high-volume manufacturing. Similarly, fluorine-containing gas plasma activation was proposed to achieve low-temperature bonding, yet the strict atmosphere control limits its adaptation in the industry.[14–16]

Recent findings highlighted the significant role of atomic diffusion in the direct bonding process, wherein atoms can migrate across or along the bonding interface during the bonding process.[17–20] According to the investigation using the embedded atom method (EAM),[21] the adatom migration on the (111) Cu surface—with its relatively low surface energy—exhibits lower activation energy compared to other crystallographic planes. This accelerated self-diffusion facilitates void densification and closure during bonding. Grain engineering leveraging (111)-oriented nt-Cu has enabled Cu—Cu bonding at ≈200 °C.[22] The unique microstructure of nt—Cu, dominated by CTBs, enhances mechanical strength, electrical conductivity, thermal stability, and resistance to electromigration (EM) and intergranular corrosion.[23,24] However, most of these nt—Cu joints exhibit a visible sharp edge with weak mechanical strength. While post-bonding annealing above 250 °C can mitigate this issue by enhancing interfacial quality, the required annealing temperature (>250 °C) still exceeds the thermal budget constraints of advanced DRAM integration technologies.

On the other hand, ng—Cu has also received attention for direct Cu—Cu bonding due to its rapid recrystallization properties, enabling grain growth across the bonding interface at a low thermal budget and yielding strong mechanical strength at the cross-interface.[25–28] However, practical challenges arise during production:plated ng—Cu undergoes several processes, including chemical mechanical polishing (CMP), wafer cutting, cleaning, and potentially transportation from the foundry site to the OSAT (Outsourced Semiconductor Assembly and Test) company. Consequently, due to the extended post-plating resting time (referred to as q-time), the grains of ng—Cu will naturally grow and coarsen even at room temperature due to the self-annealing effect.[29] This phenomenon makes the ng—Cu materials impractical for real production scenarios. Moreover, studies include highly (110)-oriented perpendicular nanotwinned Cu (p-ntCu) for bonding at 200–250 °C, although anisotropic grain growth mainly occurs laterally, resulting in voids at straight interfaces.[30] Micro-cone Cu structures fabricated by pulse electrodeposition require very high bonding pressures (≥100 MPa) to reduce void formation at 250 °C.[31] Quenching-induced wrinkled surfaces introduce strain energy but necessitate processing at 300 °C.[32] Recent work suggests a good approach using hybrid surface grains with (111)-oriented and nanocrystalline structures, which leverage rapid (111) diffusion and grain-boundary pathways to achieve bonding at 200 °C.[33]

In this work, we developed a unique composite copper (comp-Cu) structure by combining (111)-oriented nt—Cu with randomly oriented ng—Cu. This comp-Cu directly addresses the limitations of conventional low-thermal-budget approaches by achieving: 1) ambient-pressure operation (vs UHV/controlled atmosphere), and 2) full compatibility with existing thermal compression tools (vs plasma/vacuum equipment). By periodically interleaving (111)-oriented nt—Cu domains with ng—Cu regions, we engineered a self-regulating system where coherent twin boundaries act as nanoscale anchors—suppressing ng—Cu coarsening during fabrication (ΔR < 2% over 15 days)—while enabling rapid nanograin recrystallization at 170 °C (43% below conventional thermal budgets). During low-temperature bonding, the inherent instability of nanograins in ng—Cu initiates grain boundary (GB) sliding and creep, driving atomic diffusion across the interface. This process not only facilitates grain growth but also generates vacancies that enhance atomic mobility in adjacent nt—Cu regions. Critically, the accelerated diffusion supplies adatoms that migrate into interfacial voids, where they diffuse faster along the low-energy (111) planes of nt—Cu, accelerating void closure and interfacial densification. This advance resolves the long-standing trade-off between thermal stability and process scalability, offering a practical and scalable pathway for direct Cu—Cu bonding in advanced electronic packaging applications.

2. Results and Discussion

The comp-Cu and nt—Cu materials were produced by controlling the additives in the aqueous plating electrolyte. The surface micromorphology was examined using Focused Ion Beam (FIB). **Figure 1a** displays the top-view surface of the nanotwin and nanograin hybridized comp-Cu, with the orange dotted circle highlighting the area containing nanotwin domains, surrounded by the nanograin region indicated by the green dotted circle. Figure 1b and Figure S1 (Supporting Information) provide zoom-out and in cross-section image of the comp-Cu, displaying a high density of nanotwin domain in the columnar grains, marked by the orange dotted circle, adjacent to the nanograin highlighted by the green dotted circle. Figure S2 (Supporting Information) shows a cross-section image of nt—Cu, illustrating typical nanotwin columnar grains. Figure 1c presents a high-resolution image of the comp-Cu, accompanied by an inset of an electron diffraction pattern, showing the region of nanotwin lamellae surrounded by a cluster of nanograins. Grain orientations and GB distributions were analyzed by Electron Backscatter Diffraction (EBSD) for comp-Cu, nt—Cu, and coarse grain Cu, as shown in Figure 1d, Figures S3 and S4 (Supporting Information), respectively. The comp-Cu exhibits a preference for the (111) orientation, with large grains enriched in this orientation and surrounded by randomly oriented nanograins. The nt—Cu shows nearly 100% (111) orientation, while the coarse grain copper exhibits a random orientation without any specific preference. X-ray diffraction (XRD) analysis also revealed a predominant (111) orientation perpendicular to the substrate in both the nt—Cu and comp-Cu materials (Figure 1e). Note that there are other orientations present in the composite Cu due to randomly oriented nanograins. This preference for the (111) orientation can be attributed to the lower energy of (111) nuclei formation during electroplating.[34,35]
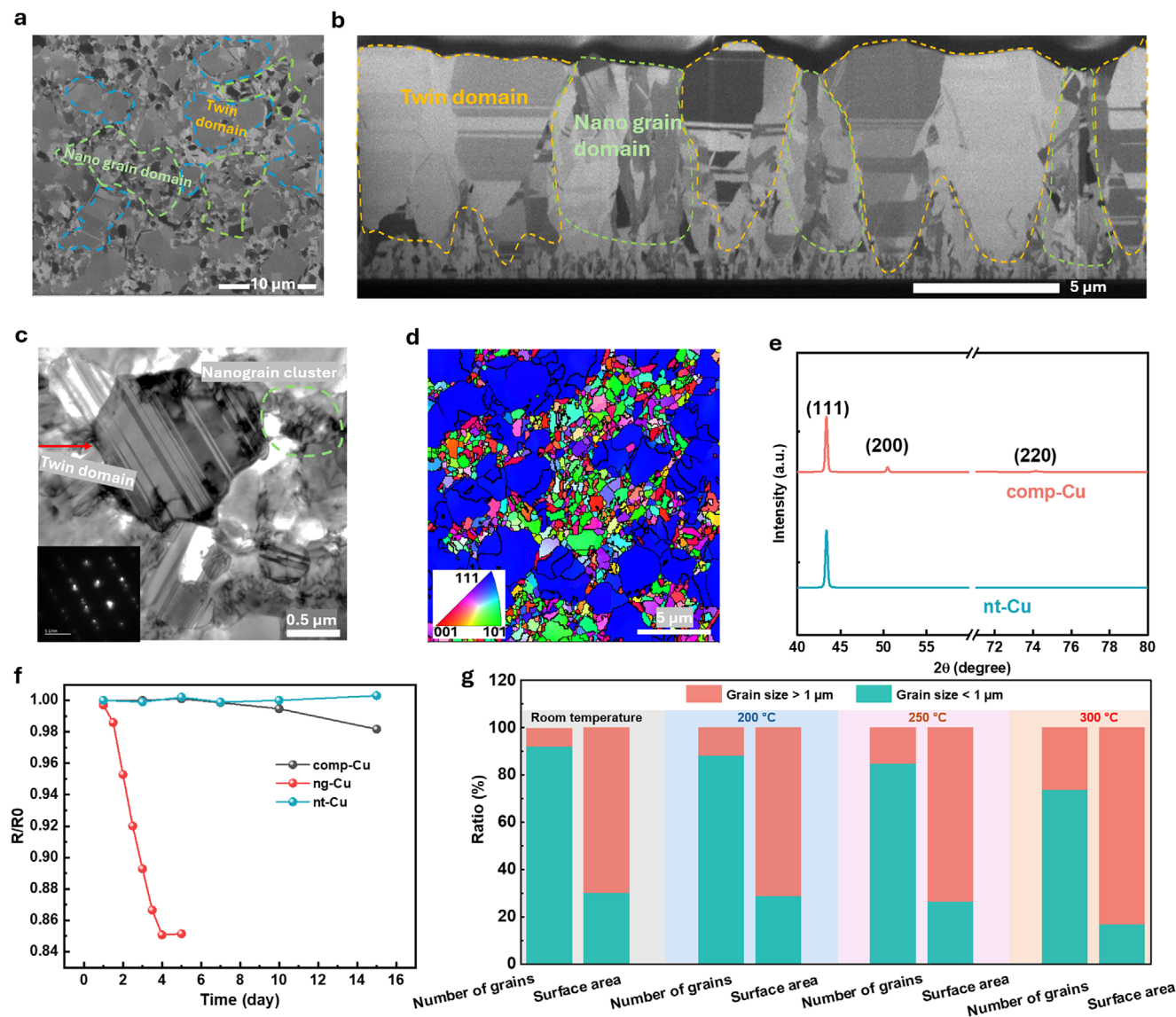
ADVANCED
SCIENCE NEWS

www.advancedsciencenews.com

small
methods

www.small-methods.com

Figure 1. Microstructure and structure stability of different copper. a) Scanning Ion Microscopy (SIM) image of top surface of comp-Cu, where the orange dotted island area is hierarchical nanotwinned domains surrounded by nanograins (green dotted lines). b) SIM image of cross section of comp-Cu. c) a high-resolution image of the comp-Cu, accompanied by an inset of an electron diffraction pattern. d) EBDS IPF-Z mapping for the comp-Cu. e) XRD of comp-Cu and nt—Cu. f) the sheet resistance changes of comp-Cu, ng—Cu (nanograin copper), and nt—Cu at room temperature. g) evolution of comp-Cu grain count ratio and surface area contribution during annealing at room temperature, 200, 250, and 300 °C for 30 min, respectively.

The structural stability of different copper samples at room temperature was assessed by monitoring changes in sheet resistance over time, as depicted in Figure 1f. The sheet resistance of ng—Cu film decreased by 15% within 5 days due to self-annealing. In contrast, the comp-Cu experienced only a 2% drop in resistance, while the resistance of nt—Cu remained nearly unchanged even after 15 days. The inhibited self-annealing phenomenon in comp-Cu can be attributed to the retardation of nanograin growth, as these grains are pinned by the high density of coherent twin boundaries. The thermal stability of the copper samples was evaluated by subjecting them to annealing at different temperatures for a duration of 30 min. The evolution of microscopic morphology and average grain size in comp-Cu was

tracked using EBSD IPF images (Figure S5, Supporting Information) and summarized in Figure 1g. In the as-deposited state, fine grains (<1 μm) made up 91.9% of the grain count but only 30.1% of the surface area, while larger grains—mostly nanotwins—covered 69.9% of the area. This disparity in size and distribution indicates notable differences between the two grain groups in the composite material. After annealing at 200 °C, fine grains slightly decreased to 87.9% of the count and 28.7% of the area, with large grains covering 71.3%. As the annealing temperature increased to 250 and 300 °C, the proportion of fine grains dropped to 84.6% and 73.5%, and their area coverage fell to 26.4% and 16.7%, respectively. Meanwhile, large grains expanded to 73.6% and 83.3% of the surface area. This grain coarsening led to an increase in
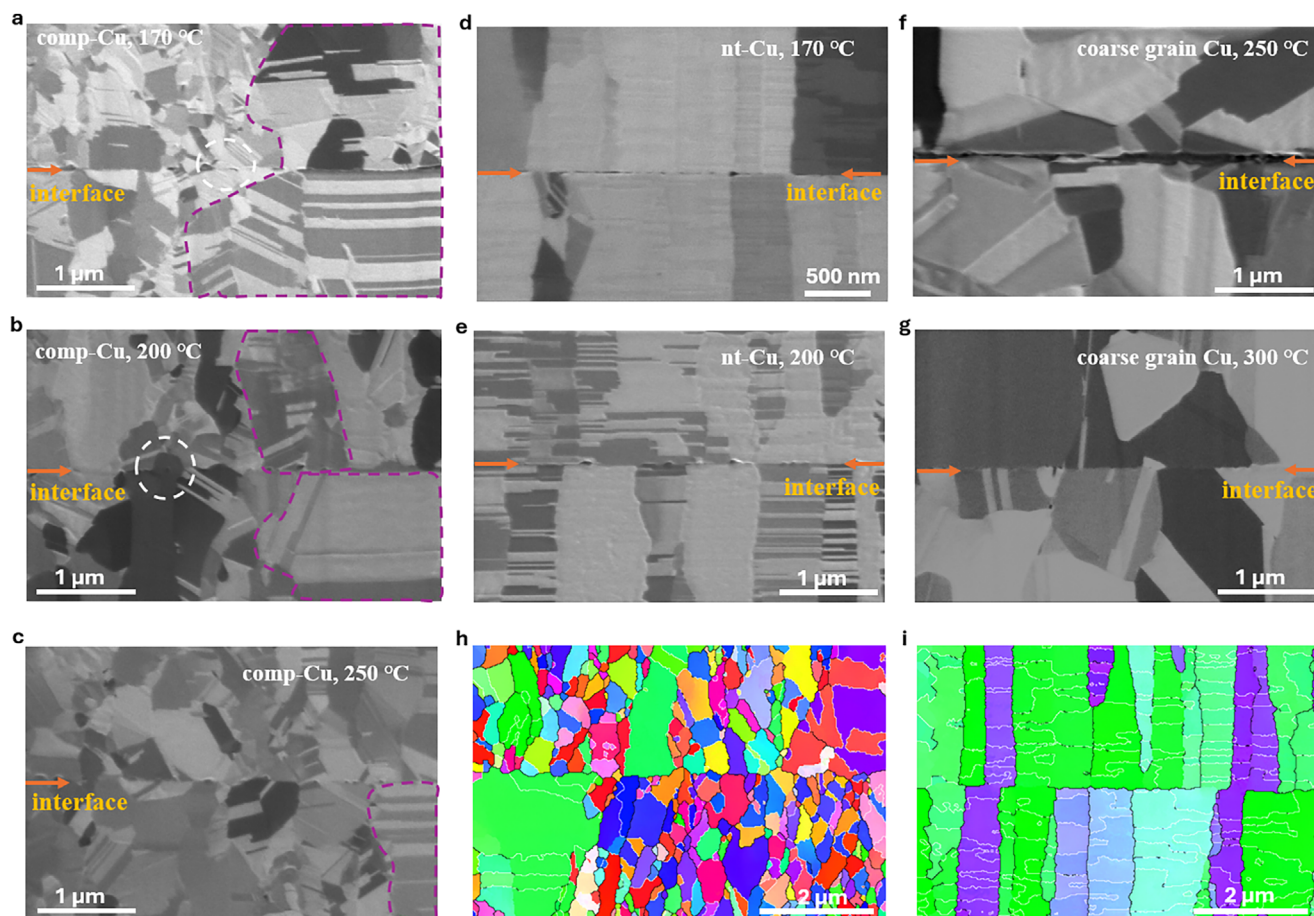
Figure 2. The interfacial characterization. a–c) SIM image of the bonding interfaces of comp-Cu bonding at 170, 200, and 250 °C, respectively. Selected nanograin-enriched regions and nanotwin areas are highlighted with purple dashed lines. d,e) bonding interfaces of nt—Cu under 170 and 200 °C. f,g) SIM images show the bonding interfaces of coarse-grain copper at 250 and 300 °C, respectively. h,i) the EBDS map for comp-Cu and nt—Cu bonded at 200 °C for 30 min.

average grain size from 427 to 515 nm at 200 °C, 666 nm at 250 °C, and 882 nm at 300 °C, suggesting that small grains merged into larger ones or combined with nanotwinned grains. In contrast, the average grain size of nt—Cu increased only slightly, from 1009 to 1045 nm (200 °C), 1095 nm (250 °C), and 1129 nm (300 °C) (Figure S6, Supporting Information).

The unique properties of comp-Cu ensure structural stability during extended periods at room temperature after electroplating while facilitating controlled grain growth at elevated temperatures during bonding processes. Theoretically, the thermodynamic driving force for grain growth is the GB energy,[36,37] and in this case, the excess energy of different copper was calculated. Table S1 (Supporting Information) presents the annealing temperatures (T), annealing times (Δt), and corresponding average grain sizes (d) for the different copper samples. Changes in average grain size were used to estimate the activation energy, with detailed calculations available in the supplementary material and Figures S7 and S8 (Supporting Information). And Tables S2 and S3 (Supporting Information) shows the results for the activation energy (Q), surface energy, and GB energy (γ_{gb}) for nt—Cu and comp-Cu. The calculated activation energy for nt—Cu is 67.34 kJ mol^{-1}, aligning with values reported in

other studies.[38–43] The activation energy for comp-Cu is 59.44 kJ mol^{-1}, slightly lower than that of nt—Cu and higher than the reported value of 35 kJ mol^{-1} for ng—Cu.[44,45] As described earlier, the composite structure comprising nanotwins and nanograins remains stable at room temperature; however, as the temperature rises, grain growth becomes more pronounced. This phenomenon could be attributed to the nanograin-enriched regions facilitating atomic movement between neighbouring nanotwins.

Subsequently, these copper samples were used for bonding comparison. Note that bonding can be classified into three types based on interfacial quality: failure bonding, successful bonding with visible interface, and successful bonding with cross-interface formation. Most current studies still show a visible interface after bonding. Enhancing cross-interface bonding or even eliminating the bonded interface is desirable especially under impact conditions such as electrical current, heat, or mechanical loading. **Figure 2**a–c shows the scanning ion microscopy (SIM) images of the bonding interfaces for the comp-Cu bonded at 170, 200, and 250 °C for 30 min, respectively. These images demonstrate successful bonding with distinct zig-zag interfaces. Notably, in the nanograin-enriched region, it can be observed that some nanograins grow across the bonding interface, which

**ADVANCED
SCIENCE NEWS**

www.advancedsciencenews.com

**small
methods**

www.small-methods.com

become more pronounced at higher bonding temperatures. As shown in Figure 2d, successful bonding can also be achieved using nt—Cu at 170 °C, forming a sharp and straight interface with the presence of voids at the interface. The bonding quality of nt—Cu can be enhanced by increasing the bonding temperature to 200 °C (Figure 2e) and 250 °C (Figure S9, Supporting Information), while still maintaining a sharp interface. In comparison, the coarse grain Cu exhibits a failure in bonding at 250 °C, with the presence of a noticeable gap shown in Figure 2f. To achieve successful bonding, a higher thermal budget of 300 °C (Figure 2g) is required for coarse-grain Cu. To further analyze the bonding interfaces, the microstructure of comp-Cu and nt—Cu bonded at 200 °C for 30 min was characterized using EBSD (Figure 2h,i). The IPF-Z mapping reveals a well-formed bonding interface with cross-interface formation in the nanograin-enriched area for comp-Cu. In contrast, nt—Cu lacks noticeable cross-interface features.

As experimentally characterized in terms of thermal stability and interfacial morphology, cross-interface growth served as the direct evidence of the excellent bonding quality in comp-Cu, which is absent in nt—Cu. This cross-interface growth region can be attributed to a combination of factors, including atomic mobility, grain boundary (GB) dynamics, and interfacial structural characteristics. First, density functional theory (DFT) calculations were performed to evaluate surface energetics. As illustrated in Figure S10 (Supporting Information) and **Figure 3a**, the (111) surface demonstrates the lowest surface energy (0.214 eV Å^{-2}) and adatom activation energy (0.942 eV) but the highest surface vacancy formation energy (0.715 eV). By comparison, the (001) surface exhibits intermediate properties, including a surface energy of 0.287 eV Å^{-2}, an adatom activation energy of 1.751 eV, and a surface vacancy formation energy of 0.287 eV. In contrast, the (011) surface displays the highest surface energy (1.018 eV Å^{-2}) and the negative surface vacancy formation energy (−0.734 eV), despite its relatively low adatom activation energy (1.674 eV). This anomalous behavior likely originates from structural instability inherent to its high-energy configuration. A more detailed discussion is in the Supporting Information. All in all, these results highlight that atoms can move more easily on the (111) surface compared to other surfaces. Consequently, atoms at the nt—Cu to nt—Cu bonded interface preferentially migrate along the X-Y interface plane, forming a straight bonding interface. DFT calculations reveal that the (111) plane has a significantly higher surface vacancy migration energy barrier (0.6053 eV) compared to the (001) (0.4398 eV) and (011) (0.2273 eV) surfaces (Figure 3b; Figure S11, Supporting Information). This elevated barrier suppresses vacancy diffusion and void aggregation at the (111) interface, hindering cross-interface growth in the Z-direction. Second, GB diffusion plays a more critical role than surface diffusion in the Z-direction bonding process.[19,46] For polycrystalline metals, the mobility of atoms along GBs is much higher than within the lattice.[47,48] As the grain size decreases, the density of GB diffusion channels increases. Consequently, comp-Cu, with an average grain size of 427 nm, exhibits more GB diffusion channels at the initial bonding interface than nt—Cu, which has an average grain size of 1009 nm. This higher density of GB channels enhances atomic migration across the interface, promoting cross-interface growth. Third, the bonding interface densifies more slowly when both

sides of the crystalline orientations are identical,[19] whereas mismatched orientations significantly accelerate densification. This enhancement arises from the randomly oriented nanograin regions in comp-Cu, which introduce interfacial GB structures and induce substantial atomic displacements at these boundaries. Furthermore, the grain growth in nanograin-enriched regions would reduce GBs, resulting in a decrease in volume and the creation of vacancies, thereby promoting atomic movement in the nearby nanotwin regions.[49,50] This enhanced atomic movement results in more adatoms migrating into cavities and voids at the bonding interface, driven by a stress potential gradient that arises between the contacted regions and the non-contacted regions along the interface.[51]

The bonding process, schematically summarized in Figure S12 (Supporting Information), involves three sequential stages. Initially, the top and bottom dies are aligned within a nitrogen chamber, resulting in two contact scenarios: 1) the (111)-dominated areas of both dies touch each other, with nanograin domains also making contact. 2) A portion of the (111) areas from the top and bottom dies overlap, resulting in large (111) areas meeting the nanograin domains. Upon applying pressure and heat, localized plastic deformation at contact points generates interfacial voids, while a stress potential gradient forms between strained contacted regions and unstrained voids. These stress potential gradient drives atomic migration from strained zones to voids, causing void coalescence and void density reduction. As shown in Figure 3c for comp-Cu bonding, void closure is driven by two primary mechanisms: GB diffusion, where atoms migrate along GBs to bonding interface (indicated by red arrows), and surface diffusion, where atoms redistribute across void surfaces (indicated by orange arrows). In the nanograin-enriched regions, GB diffusion promotes grain growth in the Z-direction and provides additional adatoms (site 1) that migrate along the X-Y bonding interface, especially at the (111)/ (111) overlap regions, where movement is faster (site 2). This atomic movement would also generate vacancies and further stimulate atomic diffusion in the adjacent nanotwin regions (site 3). As a result, the increased adatoms and their rapid migration along the bonding interface toward voids facilitate interfacial densification and promote cross-interface bonding.

Figure 3d–f shows the TEM images of the bonding interface for coarse-grain copper at 300 °C and nt—Cu and comp-Cu at 200 °C, respectively. In Figure 3d, voids along the bonding interface can be observed in the coarse-grain sample. These voids have an average diameter of ≈30 nm and a void density of 6.2/μm, where the void density is defined as the number of voids per unit length along the bonding interface. In Figure 3e, for the nt-Cu sample, large voids are present along the bonding interface, with an average diameter of ≈60 nm and a void density of 1.7/μm. In the case of comp-Cu in Figure 3f, it can be observed that nanograins exhibit growth across the interface, as indicated by the blue dashed rectangle. The voids in comp-Cu have an average diameter of ≈30 nm, with a void density of 1.5/μm. The reduced number and smaller size of voids in the comp-Cu sample provide evidence of accelerated void closure during bonding, densifying the bonding interface. Stress-driven surface diffusion (creep) also causes impurity atoms to migrate from strained areas to unstrained regions, like interfacial voids (Figure 3g–i; Figure S13, Supporting Information). TEM-EDS mapping
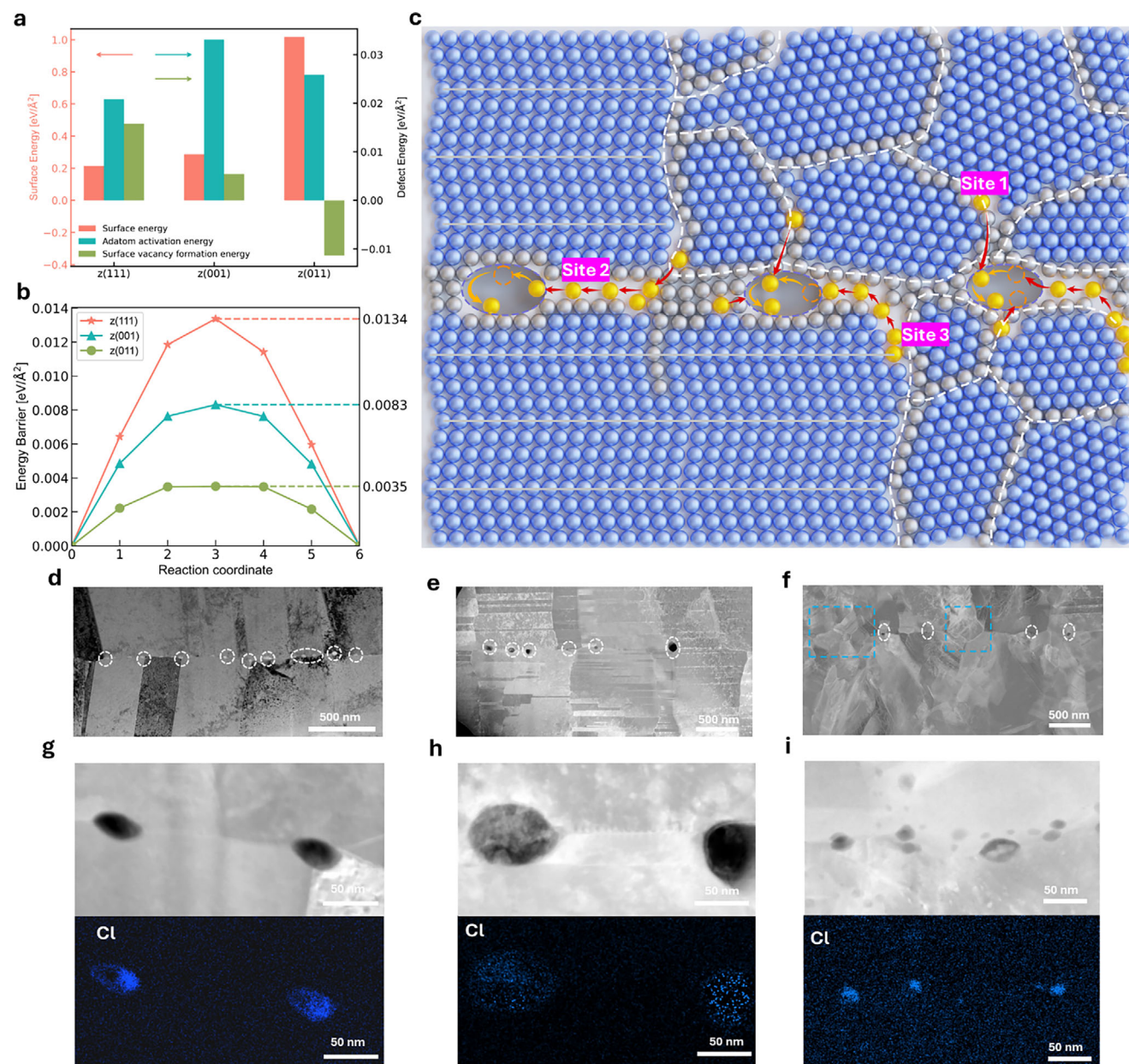
**ADVANCED
SCIENCE NEWS**

www.advancedsciencenews.com

**small
methods**

www.small-methods.com

Figure 3. Surface energy and bonding interface. a) Comparison of surface energy, adatom activation energy, and surface vacancy formation energy for slab surface models of (111), (001), and (011) along z axis. b) Comparison of surface vacancy migration energy barrier for vacancy-defected slab models of (111), (001), and (011) along z axis. c) Schematic figure illustrating voids closure of comp-Cu. d–f) TEM images depict the bonding interface of coarse-grain copper, nt—Cu, and comp-Cu, respectively, after being bonded at 300, 200, and 200 °C for 30 min respectively. In each figure, White dashed lines in (d), (e), and (f) are nano-sized voids. g–i) TEM images and Energy-Dispersive X-ray Spectroscopy (EDS) analysis were performed on the magnified bonding interfaces of three types of copper: coarse-grain copper, nt—Cu, and comp-Cu.

confirms these voids are enriched with chlorine (Cl), oxygen (O), and nitrogen (N) impurities originating from electroplating additives. Secondary ion mass spectrometry (SIMS) analysis measured the bulk impurity concentrations in the electroplated Comp-Cu films as Cl: 334.8, O: 71.65, and N: 4.73 ppm.

Apart from the morphological analysis, the distinct bonding performance of comp-Cu was evaluated in mechanical and electrical performance. Shear tests were conducted to compare the mechanical bonding strength of comp-Cu, nt—Cu, and coarse

grain copper, which were bonded at 200, 200, and 300 °C for 30 min respectively. **Figure 4a** presents the results for three sets of samples, each consisting of three parallel samples. The calculated average shear strength for comp-Cu is 56.4 ± 3.6 MPa, which is higher than that of nt-Cu (49.0 ± 4.3 MPa) and significantly higher than that of coarse-grain copper (36.9 ± 2.6 MPa). Electromigration (EM) tests were performed to evaluate the electrical performance, as shown in Figure 4b, with a representative SEM image of the circuit used for the EM test. The "dog-bone"

**ADVANCED
SCIENCE NEWS**

www.advancedsciencenews.com

**small
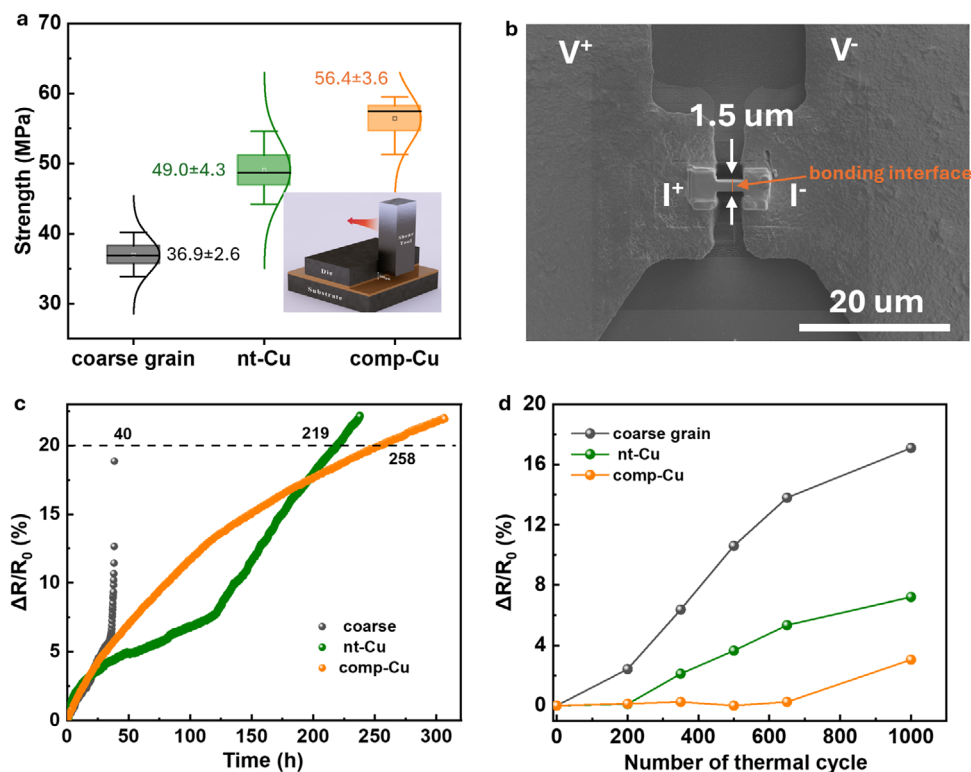methods**

www.small-methods.com

Figure 4. Evaluation of bonding performance. a) A typical shear test diagram includes samples of Comp-Cu and nt—Cu bonded at 200 °C for comparison, while coarse-grained copper bonded at 300 °C serves as the baseline reference, as coarse-grained copper cannot be bonded at 200 °C. b) plan-view SEM image of EM testing setup. c) Comparison of the resistance changes of the comp-Cu, nt—Cu, and reference coarse grain copper under EM stressing. d) Resistance changes of the comp-Cu, nt—Cu, and reference coarse-grain copper during thermal cycle testing. Temperature cycling range was set as −16 °C ≈160 °C with soak time of 5 min and Ramp rate of ≈117 °C min^{-1}.

bonding joint, with the bonding interface highlighted by a yellow dash line, was extracted from the thinned bonding die using FIB techniques. Subsequently, it was welded on the measurement stage using easy-lift tool of FIB system. To ensure protection, the measured circuits were coated with a 30 nm thick Pt layer and subjected to a continuous current density of 3×10^6 A cm^{-2} on a hotplate at 165 °C. The electrical resistance changes over time were recorded using a four-point probe system during the EM test. The EM lifetime was defined as the duration of time which the resistance increases by 20%. The corresponding resistance changes curves are presented in Figure 4c. The comp-Cu sample exhibited a lifetime of 258 h, which is 6.45 times longer than that of coarse copper (40 h) and 1.18 times longer than nt-Cu (219 h). The improvement in EM resistance in the comp-Cu can be attributed to two factors. First, the presence of (111)-oriented nanotwin Cu in the composite structure contributes to enhanced resistance to EM. Second, the nanograin-enriched region undergoes grain growth and enhance cross-bonding interface formation, serving as a tenon to reinforce the bonding quality. Following the EM test, the microstructure was examined using FIB to gain insights into the failure mechanism. In the case of the coarse-grain copper samples (Figure S14a, Supporting Information), numerous voids are observed at the bonding interface and within the internal area. These voids result from the agglomerations of vacancies, which easily form and grow at weak points, especially the bonding interfaces. As previously de-

scribed, relatively large voids were formed at the bonding interface of the nt—Cu sample, representing the weak points that are expected to undergo further growth under prolonged electrical stress (Figure S14b, Supporting Information). In contrast, for the comp-Cu (Figure S14c, Supporting Information), only small voids (highlighted by a yellow dashed circle) are visible at GBs located away from the bonding interface. The findings suggest that the enhanced cross-interface formation improves the contact performance, making it more comparable to that of bulk Cu. The presence of more voids at GBs near the bonding interface after EM test may be attributed to the accumulation of higher impurity levels in the vicinity of the bonding interface. To further evaluate the bonding quality, temperature cycling tests (TCT) were conducted with a temperature range of −16 to 160 °C, a soak time of 5 min, and a ramp rate of ≈117 °C per min. As shown in Figure 4d, after 1000 cycles, the resistance of the comp-Cu sample increased by 3.1%, while the nt—Cu sample exhibited an increase of 7.2%, and the coarse grain Cu sample displayed a significant increase of 17.1%. The cross-sections of the samples after TCT were analysed by FIB (Figure S15, Supporting Information). In the case of the coarse grain and nt—Cu dies, cracks were observed at the bonding interface, indicating that the failure initiated at the bonding interface due to a weak point. Conversely, in the comp-Cu sample, cracks primarily formed at GBs, suggesting that the bonding interface exhibits strength comparable to the bulk Cu body in the circuit.

**ADVANCED
SCIENCE NEWS**

www.advancedsciencenews.com

**small
methods**

www.small-methods.com

3. Conclusion

In this study, we fabricated a unique comp-Cu structure by hybridizing (111)-oriented nanotwin and randomly oriented nanograin structures. We investigated the thermal stability and activation energy of grain growth, demonstrating direct Cu—Cu bonding at temperatures below 200 °C with enhanced mechanical and electrical performances. The bonding quality of comp-Cu exhibited better mechanical strength, EM lifetime, and TCT performance compared to nt—Cu and coarse grain Cu. This composite structure offers three key advantages. First, the composite structure remains stable at room temperature and undergoes substantial grain growth when exposed to elevated temperatures. The presence of twin boundaries in this composite structure acts as a pinning mechanism, suppressing the self-annealing effect of the nanograin structure during extended processing periods after electroplating and before bonding. Second, the composite retains the advantages of (111) oriented nanotwin structures, such as higher resistance to EM. Third, under low-temperature conditions, the nanograin-enriched regions can enhance grain growth and also promote atomic movement between adjacent nanotwins across the bonding interface. Moreover, the enhanced atomic movement generates more adatoms migrating along the bonding interface toward voids, especially at a faster rate on the (111)-oriented surface, thereby facilitating interfacial densification. The combination of stability at room temperature and cross-interface bonding at low temperatures presents a practical approach for real-world industrial manufacturing in advanced microelectronic packaging.

4. Experimental Section

Electroplating Process: A copper electroplating bath was prepared with 0.6 M $CuSO_4 \cdot 5H_2O$, 90 g L^{-1} H_2SO_4 (Sigma–Aldrich), 40 ppm HCl (Sigma–Aldrich), and proprietary additives (accelerators/suppressors, Doctech Ltd., Hong Kong SAR, China). Electrodeposition was performed on a silicon substrate pre-coated with a 100 nm Ti adhesion layer and 200 nm Cu seed layer, using a phosphorus-doped copper anode. By systematically tuning the type and ratio of accelerators and suppressors within the additive packages, three distinct types of copper films were selectively deposited: ng—Cu, Comp-Cu, and nt—Cu.

In this study, the effects of plating parameters on the copper microstructure were investigated. It was found that changing the current density from 3 to 7 ASD had little impact, so a fixed value of 5 ASD was used. The microstructure was mainly affected by the accelerator concentration. The suppressor level was kept constant, and the accelerator amount was adjusted. As shown in Figure S16 (Supporting Information), at low accelerator levels (1–4 μL), large nanotwinned grains with few nanograins were formed. When the accelerator increased moderately, nanograins appeared within the nanotwinned grains, forming the desired composite structure. With further increases, the grain size became smaller, and a fully nanograined structure was obtained.

The comp-Cu microstructure arises from the dynamic interplay between a polymeric suppressor and a sulfur-based accelerator. The suppressor strongly adsorbs onto the Cu surface under steady-state conditions, inhibiting deposition particularly in field regions, while the accelerator locally promotes deposition in recessed areas. Crucially, during the plating process, the suppressor undergoes periodic adsorption and desorption, driven by local fluctuations in electric field and additive transport. This dynamic modulation of the electrochemical potential—somewhat analogous to the transient conditions in pulse-reverse plating—creates a non-equilibrium environment that favors the co-deposition of twin boundaries and nanocrystalline copper domains.[52]

Microstructure Characterization: The top surface and cross-section microstructures of different copper films were characterized using focused ion beam (FIB, Quanta 200 3D and Helios Nano lab 600i, FEI), transmission electron microscope (STEM, Thermo Scientific Talos F200X), and electron backscatter diffraction (EBSD, Oxford HKL Channel 5). Crystal structure of Cu film was characterized by X-ray Diffractometer (XRD, Rigaku SmartLab, Cu-Kα). The average grain size of the electroplated copper film after chemical mechanical polishing (CMP) was analyzed using (EBSD). The sheet resistance of the copper film was measured using the four-point probe method.

Direct Cu—Cu Bonding: After the copper deposition on the silicon wafer, the CMP process was performed to flatten the copper surface. Then, the copper wafer was cut into a small die (≈0.5 × 0.5 cm) and cleaned with acetone, isopropanol, acid solution (HCl: DI water = 1:1 in vol.%), and deionized water. Finally, the copper surface was further cleaned by plasma with nitrogen atmosphere, and it was quickly transferred to a closed chamber for bonding. The bonding parameters were set as 170–300 °C/30 MPa/30 min, 230 Pa vacuum.

Bonding Quality Characterization—Micromorphology of the Bonding Interface: The bonding interface was analysed using a combination of FIB, EBSD, STEM, and SEM.

Bonding Quality Characterization—Mechanical Strength: Shear tests were conducted by bonding a small top die with a Cu film to a larger bottom die, also coated with a Cu film. The top die measured 6 mm × 6 mm, while the bottom die was 10 mm × 10 mm. Both dies were deposited with a 6 μm-thick copper film, followed by CMP, plasma surface activation, and vacuum bonding. Shear tests were performed at a speed of 80 μm s^{-1}, with 4 samples tested in each group.

Bonding Quality Characterization—Electromigration and Thermal Cycling Assessments: Auxiliary Cu circuits were first fabricated on a Si/Ti/Cu seed layer using photolithography and electroplating, followed by photoresist removal and seed layer etching. The bonded copper dies were then thinned by rotary grinding. Cuboid columns (2.5 × 3 × 10 μm^3) containing the bonding interface were milled using FIB and welded onto the circuit via tungsten deposition. These columns were subsequently etched into dog-bone structures with a neck width of 1.5 μm for testing. Notably, Comp-Cu bonded cuboid columns were deliberately selected to include a cross-interface area, while nt—Cu bonded columns featured a straight bonding interface.

Electromigration tests were conducted at 165 °C by applying a constant current corresponding to a current density of 3 × 10^6 A cm^{-2} to the cuboid columns. The increase in resistance was monitored indirectly by measuring the voltage rise using a four-point probe. Thermal cycling tests were performed between −16 and 160 °C, with 5 min dwell times at each temperature extreme and a ramp rate of 117 °C min^{-1}.

Density Functional Theory Calculation: DFT calculation details can be found in the subsection Surface properties calculation with DFT in the Supporting Information.

Statistical Analysis: Shear tests were conducted at a speed of 80 μm s^{-1}, with four samples (each measuring 6 mm × 6 mm) tested per bonding condition. Results were reported as mean ± standard deviation (SD). For electromigration and thermal cycling assessments, individual samples were carefully prepared with well-defined bonding interfaces and evaluated following standard microfabrication and FIB processing. To facilitate comparison across conditions, all measured data were normalized. Statistical analysis and data visualization were performed using OriginPro 2023.

Supporting Information

Supporting Information is available from the Wiley Online Library or from the author.

Acknowledgements

Conflict of Interest

The authors declare no conflict of interest.

Author Contributions

C.C. and H.L. contributed equally to this work. S-P.F., C.C., and Y.T.H. conceived the idea and designed experimental schemes. C.C., H.Y.L, G.Q.P, Z.Y.Z, E.Q.D., J.W.Z., Y.W., C.H. and Y.T.H developed methodology and experimental characterization. H.Y.L., J.S.C and C.M.C. perform related calculations. C.C., S-P.F., H.Y.L., C.M.C., and Z.F.G. analyzed the data. C.C. and H.Y.L. drew figures and co-wrote the manuscript with all the other authors. S.P.F., C.M.C., J.W.G., and Y.T.H. supervised the work. S-P.F., H.Y.L., C.M.C., J.W.G., and Y.T.H. conduct a major revision of the manuscript, and all authors discussed and commented on the manuscript.

Data Availability Statement

The data that support the findings of this study are available in the supplementary material of this article.

Keywords

[1] R. Chen, Y. C. Li, J. M. Cai, K. Cao, H. B. R. Lee, Atomic Level Deposition to Extend Moore's Law and Beyond. International Journal of Extreme Manufacturing. IOP Publishing Ltd June 1 **2020**, *2*, 022002.

[2] H. T. Kung, presented at *Real-Time Signal Processing III San Diego* **1980**, Vol. *241*, pp. 76–84.

[3] T. Wei, J. Cai, Q. Wang, Z. Liu, Y. Li, T. Wang, D. Wang, presented at *2012 13th Int.Conf. on Electronic Packaging Technology & High Density Packaging*, IEEE, Guilin, China **2012**.

[4] M. Datta, *J. Micromanuf.* **2020**, *3*, 69.

[5] D. H. Cho, S. M. Seo, J. B. Kim, S. H. Rajendran, J. P. Jung, *Metals (Basel)* **2021**, *11*, 1664.

[6] S. Son, J. Min, E. Jung, H. Kim, T. Kim, H. Jeon, J. Kim, S. Kim, K. Moon, K. Na, K. Hwang, G. Y. Yeom, presented at *Proceedings – Electronic Components and Technology Conference*, Institute of Electrical and Electronics Engineers Inc, Orlando, FL, USA **2020**.

[7] L. Wang, G. Fountain, B. Lee, G. Gao, C. Uzoh, S. Mcgrath, P. Enquist, S. Arkalgud, L. Mirkarimi, presented at *Pan Pacific Microelectronics Symposium*, IEEE, Kauai, HI **2017**.

[8] C. S. Tan, R. Reif, N. D. Theodore, S. Pozder, *Appl. Phys. Lett.* **2005**, *87*, 1.

[9] B. Rebhan, T. Plach, S. Tollabimazraehno, V. Dragoi, M. Kawano, presented at *22014 Inter. Conf. on Electronics Packaging (ICEP)*, IEEE, Toyama, Japan **2014**.

[10] H. Han, C. Lee, Y. Kim, J. Lee, R. Kim, J. Kim, B. Yoo, *Appl. Surf. Sci.* **2021**, *550*, 149337.

[11] T. H. Kim, M. M. R. Howlader, T. Itoh, T. Suga, *J. Vac. Sci. Technol., A* **2003**, *21*, 449.

[12] A. Shigetou, N. Hosoda, T. Itoh, T. Suga, presented at *51st Electronic Components and Technology Conference*, IEEE, Orlando, FL, USA **2001**.

[13] A. Shigetou, T. Itoh, M. Matsuo, N. Hayasaka, K. Okumura, T. Suga, *IEEE Transactions on Advanced Packaging* **2006**, *29*, 218.

[14] N. Watanabe, T. Asano, *Appl. Phys. Express* **2011**, *4*, 016501.

[15] D. D. Coolbaugh, L. J. Matienzo, F. D. Egitto, A. R. Knoll, *Surf. Interface Anal.* **1990**, *15*, 119.

[16] J. Tang, J. B. J. Schelen, C. I. M. Beenakker, *ECS Trans.* **2011**, *34*, 913.

[17] K. C. Chen, W. W. Wu, C. N. Liao, L. J. Chen, K. N. Tu, *Science* **2008**, *321*, 1066.

[18] T. Shimatsu, M. Uomoto, *J. Vac. Sci. Technol., B* **2010**, *28*, 706.

[19] H. Tatsumi, C. R. Kao, H. Nishikawa, *Sci. Rep.* **2023**, *13*, 23030.

[20] C. D. Breach, F. W. Wulff, *Microelectron. Reliab.* **2010**, *50*, 1.

[21] P. C. Liu, J. Cohen, J. Adams, A. Voter, *Surf. Sci.* **1991**, *253*, 334.

[22] C. M. Liu, H. W. Lin, Y. S. Huang, Y. C. Chu, C. Chen, D. R. Lyu, K. N. Chen, K. N. Tu, *Sci. Rep.* **2015**, *5*, 1.

[23] X. Zhao, C. Lu, A. K. Tieu, L. Pei, L. Zhang, K. Cheng, M. Huang, *Mater. Sci. Eng., A* **2016**, *676*, 474.

[24] Y. J. Li, K. N. Tu, C. Chen, *Materials* **2020**, *13*, 1211.

[25] Y. Wang, Y. T. Huang, Y. X. Liu, S. P. Feng, M. X. Huang, *Scr. Mater.* **2022**, *220*, 114900.

[26] J. J. Jhan, K. Wataya, H. Nishikawa, C. M. Chen, *J. Taiwan Inst. Chem. Eng.* **2022**, *132*, 104127.

[27] C. He, J. Zhou, R. Zhou, C. Chen, S. Jing, K. Mu, Y. T. Huang, C. C. Chung, S. J. Cherng, Y. Lu, K. N. Tu, S. P. Feng, *Nat. Commun.* **2024**, *15*, 7095.

[28] C.-N. Li, W.-L. Chiu, H.-H. Chang, C. Chen, presented at *2024 International Conference on Electronics Packaging (ICEP)*, IEEE, Toyama, Japan **2024**.

[29] C. E. Ho, C. C. Chen, M. K. Lu, Y. W. Lee, Y. S. Wu, *Surf. Coat. Technol.* **2016**, *303*, 86.

[30] H. Li, Z. Liang, Z. Ning, Z. Liu, M. Li, Y. Wu, *Mater. Charact.* **2024**, *217*, 114455.

[31] M. Zhang, L. Y. Gao, Y. X. Wang, W. Dong, N. Zhao, Z. Q. Liu, *Appl. Surf. Sci.* **2024**, *650*, 159184.

[32] T. F. Lu, Y. T. Yen, P. W. Wang, Y. F. Cheng, C. H. Chen, Y. C. S. Wu, *Nanomaterials* **2024**, *14*, 861.

[33] C. N. Li, J. J. Ong, W. L. Chiu, S. C. Yang, H. H. Chang, C. Chen, presented at *Proceedings – Electronic Components and Technology Conference*, Institute of Electrical and Electronics Engineers Inc, Piscataway, New Jersey, USA **2024**.

[34] D. Grujicic, B. Pesic, *Electrochim. Acta* **2002**, *47*, 2901.

[35] B. Hong, C. Jiang, X. Wang, *Surf. Coat. Technol.* **2007**, *201*, 7449.

[36] N. Nafsin, J. A. Aguiar, T. Aoki, A. M. Thron, K. van Benthem, R. H. R. Castro, *Acta Mater.* **2017**, *136*, 224.

[37] S. Dey, C. H. Chang, M. Gong, F. Liu, R. H. R. Castro, *J. Mater. Res.* **2015**, *30*, 2991.

[38] R. Niu, K. Han, Y. F. Su, T. Besara, T. M. Siegrist, X. Zuo, *Sci. Rep.* **2016**, *6*, 31410.

[39] N. Alshwawreh, M. Militzer, D. Bizzotto, *J. Electron. Mater.* **2010**, *39*, 2476.

[40] T. Sharma, P. Shaver, D. A. Brown, R. Brüning, V. Peldzinski, A. Ferro, *Electrochim. Acta* **2016**, *196*, 479.

[41] S. K. Donthu, M. M. Vora, S. K. Lahiri, C. V. Thompson, S. Yi, *J. Electron. Mater.* **2003**, *32*, 531.

[42] K. B. Yin, Y. D. Xia, C. Y. Chan, W. Q. Zhang, Q. J. Wang, X. N. Zhao, A. D. Li, Z. G. Liu, M. W. Bayes, K. W. Yee, *Scr. Mater.* **2008**, *58*, 65.

[43] L. Lu, L. B. Wang, B. Z. Ding, K. Lu, *Mater. Sci. Eng.* **2000**, *286*, 125.

[44] S. Simoes, R. Calinas, M. T. Vieira, M. F. Vieira, P. J. Ferreira, *Nanotechnology* **2010**, *21*, 145701.

[45] M. R. Akbarpour, H. S. M. Kim, *Mater. Des.* **2015**, *83*, 644.

[46] B. Rebhan, K. Hingerl, *J. Appl. Phys.* **2015**, *118*, 135301.

[47] K. N. Tu, *J. Appl. Phys.* **2003**, *94*, 5451.

[48] J. Zhou, V. Mohles, *Acta Mater.* **2011**, *59*, 5997.

[49] C. Chen, S. J. Cherng, C. He, C. C. Chung, S. Wang, Y. T. Huang, S. P. Feng, *J. Mater. Res. Technol.* **2023**, *27*, 4883.

[50] D. A. Reed, G. Ehrlich, *Surf. Sci.* **1981**, *102*, 588.

[51] J. Y. Juang, C. L. Lu, Y. J. Li, P. N. Hsu, N. T. Tsou, K. N. Tu, C. Chen, *J. Mater. Res. Technol.* **2021**, *14*, 719.

[52] L. Lu, Y. Shen, X. Chen, L. Qian, K. Lu, *Science* **2004**, *304*, 422.